

# Regulating Electronic Structure of SingleAtom Catalysts toward Efficient Bifunctional Oxygen Electrocatalysis

J. Ji, L. Ma

To be published in "Small Methods"

February 2022

Photon Sciences

**Brookhaven National Laboratory**

**U.S. Department of Energy**

USDOE Office of Science (SC), Basic Energy Sciences (BES) (SC-22)

Notice: This manuscript has been authored by employees of Brookhaven Science Associates, LLC under Contract No.DE-SC0012704 with the U.S. Department of Energy. The publisher by accepting the manuscript for publication acknowledges that the United States Government retains a non-exclusive, paid-up, irrevocable, world-wide license to publish or reproduce the published form of this manuscript, or allow others to do so, for United States Government purposes.

## **DISCLAIMER**

This report was prepared as an account of work sponsored by an agency of the United States Government. Neither the United States Government nor any agency thereof, nor any of their employees, nor any of their contractors, subcontractors, or their employees, makes any warranty, express or implied, or assumes any legal liability or responsibility for the accuracy, completeness, or any third party's use or the results of such use of any information, apparatus, product, or process disclosed, or represents that its use would not infringe privately owned rights. Reference herein to any specific commercial product, process, or service by trade name, trademark, manufacturer, or otherwise, does not necessarily constitute or imply its endorsement, recommendation, or favoring by the United States Government or any agency thereof or its contractors or subcontractors. The views and opinions of authors expressed herein do not necessarily state or reflect those of the United States Government or any agency thereof.

## Regulating electronic structure of single-atom catalysts towards efficient bifunctional oxygen electrocatalysis

*Jiapeng Ji, Lei Wu, Shiyu Zhou, Tong Qiu, Zeheng Li, Liguang Wang\*, Liang Zhang, Lu Ma, Min Ling\*, Shaodong Zhou\*, Chengdu Liang*

J. Ji and L. Wu contributed equally to this work.

J. Ji, L. Wu, S. Y. Zhou, T. Qiu, Z. Li, L. Wang, M. Ling, S. Zhou, C. Liang  
Zhejiang Provincial Key Laboratory of Advanced Chemical Engineering Manufacture  
Technology, College of Chemical and Biological Engineering, Zhejiang University,  
Hangzhou 310027, China  
E-mail: lgwang.hit@gmail.com (L. Wang); minling@zju.edu.cn (M. Ling);  
szhou@zju.edu.cn (S. Zhou).

L. Wang, M. Ling  
Institute of Zhejiang University-Quzhou, 78 Jiu Hua Boulevard North, Quzhou 324000, China

L. Zhang  
Institute of Functional Nano & Soft Materials (FUNSOM), Jiangsu Key Laboratory for  
Carbon-Based Functional Materials & Devices, Joint International Research Laboratory of  
Carbon-Based Functional Materials and Devices, Soochow University, Suzhou 215123,  
Jiangsu, China

L. Ma  
National Synchrotron Light Source II, Brookhaven National Laboratory, Upton, New York  
11973, United States

**Keywords:** single-atom catalysts, electronic structure regulation, binding energy, synergistic effect, bifunctional oxygen electrocatalysis

**Abstract:** Electronic structure of single-atom catalysts (SACs) is critical for bifunctional oxygen electrocatalysis by adjusting the binding energy in oxygen-containing intermediates. However, the regulation of electronic structure has always been a challenge to improve catalytic reactivity. Herein, by introducing a heterogenous metal, we effectively adjust the electronic structure through a direct bonding interaction to the active center atom. Partial charge transfer between the two atoms optimizes the binding energy of intermediates and reducing the energy barrier of the catalytic reaction. Theoretical calculations confirm these effects and the uniform distribution of 3d orbitals, leading to the improvement of bifunctional oxygen electrocatalytic reactivity. Benefiting from these attributes, the as-constructed bifunctional catalyst enables outstanding electrocatalytic performances in both oxygen reduction and hydrogen oxidation in

various energy storage systems. We also demonstrate the generality and expandability of this strategy by further successfully development of other dual-metal catalysts systems with various active metals.

## 1. Introduction

To overcome the slow kinetics of reversible oxygen reactions, tremendous efforts have been devoted to searching for low-cost and high-efficiency catalysts, including carbon-based, transition metal-based catalysts and their coupling composites.<sup>[1]</sup> Among them, single-atom catalysts (SACs) have attracted great research interest due to their maximum atom utilization, well-defined active sites, and tunable electronic structures.<sup>[2]</sup> However, limited by the scaling relationships between the binding energies of oxygen-containing intermediates in the four-electron steps of oxygen electrocatalysis, there is still a challenge to achieve efficient oxygen reduction reaction (ORR) and oxygen evolution reaction (OER) activities simultaneously.<sup>[3]</sup> Generally, the increase of activity on one side is often offset by the decrease of activity on the other side. Therefore, it remains a challenge to optimize the binding energy of intermediates and accelerate the kinetics of oxygen electrocatalysis by rational design of the active centers of SACs.

The electronic structure of SACs determines the adsorption energy of the oxygen-containing intermediates and catalytic properties of reversible oxygen reactions.<sup>[4]</sup> In order to optimize the electronic structure of SACs, tremendous strategies have been developed to modulate the coordination environment of single-atom sites, i.e., interactions with the substrate by changing the central transition metal atom, peripheral ligands or the crystallographic surface of the substrate,<sup>[5]</sup> the coordination number of metal atoms,<sup>[6]</sup> the doped heteroatoms (N, P, S, etc.),<sup>[7]</sup> and compressive strain.<sup>[8]</sup> However, the aforementioned electronic structure adjustment strategies at single-atom sites have limited improvement in the bifunctional oxygen electrocatalytic performance. Recent studies have shown that the doping of different single-

atom components with ORR activity and OER activity in the same substrate can produce synergistic effects to achieve high-performance reversible oxygen electrocatalysis.<sup>[3,9]</sup> Nevertheless, there is a challenge for achieving direct atomic interaction between the single-atom active center with heterogeneous atoms, while such direct interaction is closely correlated to the single-atom electronic structure that determines its bifunctional oxygen electrocatalytic reactivity.

Herein, we report an electronic structure regulating strategy through a two-step chelating-adsorbing method for introducing a heterogeneous metal that can directly interact with the center single atoms. Advanced synchrotron-based X-ray absorption fine structure (XAFS) measurements give direct evidence for the atomic distribution of metals (Fe and Co) on the nitrogen-doped graphene and the exist interaction between the metals. Heterogeneous Co atom regulates the electronic structure of the Fe single-atom catalyst. The presence of charge transfer between Fe-N<sub>x</sub>/C and Co-N<sub>x</sub>/C and a more uniform distribution of Fe 3d orbital optimize the binding energy of the intermediates and reduce the energy barrier of the rate-limiting step in the bifunctional oxygen electrocatalysis process. As a result, Fe-N/G-Co catalyst has outstanding performance of oxygen reduction reaction ( $E_{\text{onset}}$ , 0.97 V;  $E_{1/2}$ , 0.85 V), oxygen evolution reaction ( $\eta_{10}$ , 440 mV), and rechargeable Zn-air batteries (gravimetric capacity, 808.9 mAh g<sub>Zn</sub><sup>-1</sup>; gravimetric energy, 952.8 Wh kg<sub>Zn</sub><sup>-1</sup>), which is better than individual Fe-N/G and N/G-Co catalysts, and commercial Pt/C+RuO<sub>2</sub>. We further verified the synergistic effect among M<sub>1</sub>-M<sub>2</sub> (M<sub>1</sub> = Fe, Mn; M<sub>2</sub> = Co, Rh, Ni, Fe) dual-metal atoms, indicating the generality and expandability of this strategy.

## 2. Results and Discussion

### 2.1. Synthesis and structural Characterization of Fe-N/G-Co

The synthetic procedure of Fe-N/G-Co involves a two-step method of co-pyrolysis and impregnation-reduction (**Figure 1a**). In brief, Fe ions were combined with EDTA-2Na to prepare Fe-EDTA chelates. Six-coordinated Fe-O<sub>4</sub>N<sub>2</sub> structures are existent in the precursors

of Fe-EDTA chelates.<sup>[10]</sup> Follow-up pyrolysis in the presence of melamine and NaCl/KCl led to the carbonization and reconstruction of the melted EDTA and the release of CO<sub>2</sub>, endowing the final products with porosity and high specific surface.<sup>[11]</sup> A large amount of nitrogen from both EDTA and melamine is retained in the carbon matrix, ensuring a high nitrogen content and anchoring metal atoms in the pre-product (denoted as p-Fe-N/G). Then the derived porous carbon was used as a host to adsorb additional Co source followed by a subsequent thermal activation for introducing Co-N active sites in the final Fe-N/G-Co catalyst. In the process, amorphous carbon is reduced for repairing the carbon structure.<sup>[12]</sup> The addition of H<sub>2</sub>O<sub>2</sub> can strip graphene-nanosheets (GNS) and reduce its agglomeration, increasing mass transport during catalytic processes.<sup>[13]</sup>

The morphology of the samples was characterized by scanning electron microscope (SEM). The morphologies of Fe-N/G-Co, Fe-N/G, N/G-Co and N/G are similar to that of GNs (Figure 1b and **Figure S1**). Transmission electron microscope (TEM) images further reveal that Fe-N/G-Co catalyst presents a 2D geometrically lamellar structure with micron-sized planar area (**Figure S2**). No metal-derived nanoparticles are detected in high resolution TEM (HRTEM) except for the lattice stripes and wrinkled surfaces associated with the primary geometrical characteristic of graphene-like analogues. The corresponding ring-like selected area electron diffraction (SAED) pattern of an individual tube illustrates its partial crystallinity.<sup>[14]</sup>

X-ray powder diffraction (XRD) patterns confirm the formation of graphene carbon in Fe-N/G-Co and controlled samples during pyrolysis. As shown in Figure 1c, a broad peak centers at 25.3° is observed, corresponding to the characteristic peaks of graphene and implying the accumulation of graphene is not neat.<sup>[11b,15]</sup> No diffraction peaks of metal crystals are observed, excluding the undesirable formation of metal particles and aggregates. Raman results further indicate that the carbon framework is composed of thin layers of graphene, as all the samples displayed two sharp peaks located around 1349 and 1583 cm<sup>-1</sup>, and a broad peak around 2700 cm<sup>-1</sup>, which correspond to the D, G, and 2D bands of carbon, respectively (Figure 1d). The

lower  $I_D/I_G$  band intensity ratios of Fe-N/G-Co and N/G-Co than Fe-N/G and N/G indicate the Co introduced in the second adsorption step can increase the extent of graphitization in the resulting carbon structures (Table S1).<sup>[12,16]</sup>

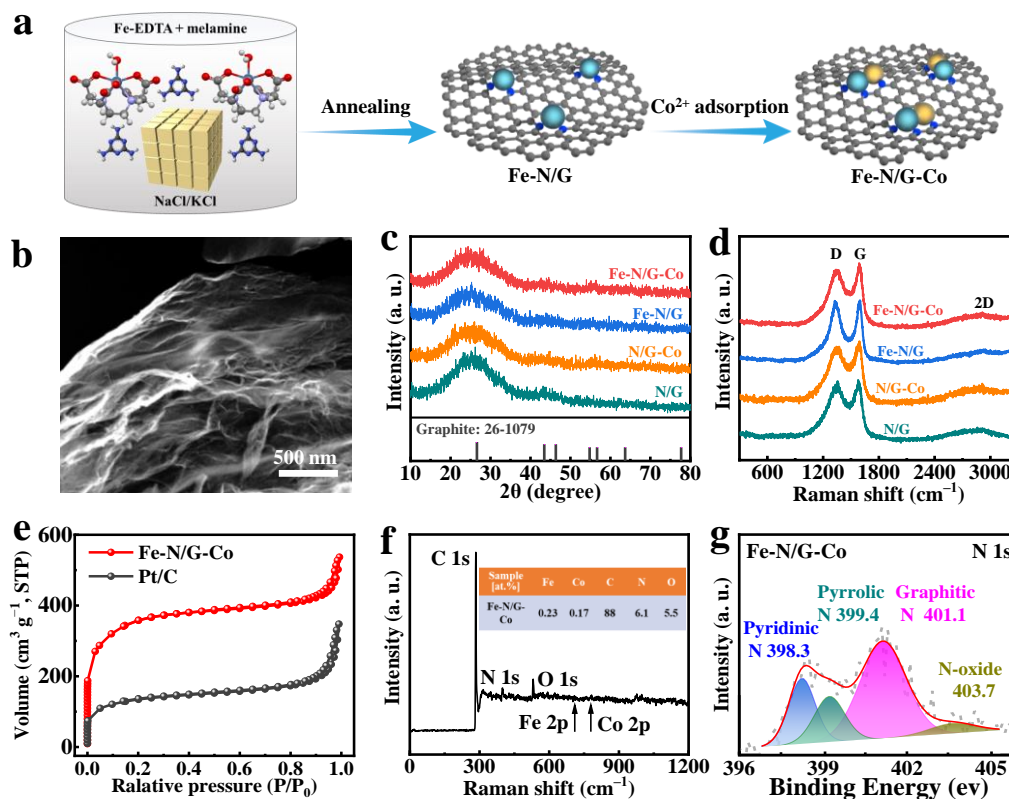


**Figure 1.** Synthesis and structural characterization of the Fe-N/G-Co. (a) Schematic illustration of the synthesis of the dual-metal active sites atomically dispersed in nitrogen doped graphene-nanosheets. (b) SEM image of the Fe-N/G-Co sample. XRD (c) and Raman (d) patterns of Fe-N/G-Co, Fe-N/G, N/G-Co and N/G samples. Standard PDF card of the Graphite (JCPDS No.26-1079) was given as reference. (e)  $N_2$  adsorption-desorption isotherms. XPS survey (f) and high-resolution spectra of N 1s (g) in Fe-N/G-Co.

The Nitrogen adsorption-desorption isotherm and corresponding pore-size distributions indicate that Fe-N/G-Co possesses an ultrahigh Brunauer-Emmett-Teller (BET) surface area of  $1086.7 \text{ m}^2 \text{ g}^{-1}$ , a meso-porous size distribution centered at  $\sim 2.22 \text{ nm}$  and a total pore volume of  $0.603 \text{ cm}^3 \text{ g}^{-1}$ , which is in sharp contrast with commercial Pt/C (Figure 1e, **Figure S3** and Table S2). Compositional analysis by X-ray photoelectron spectroscopy (XPS) and inductively coupled plasma atomic emission spectroscopy (ICP-AES) reveals that the nitrogen and metal contents of Fe-N/G-Co are  $\sim 6.1 \text{ atom\%}$  and  $\sim 0.2 \text{ atom\%}$  (Figure 1f&g, **Figure S4** and Tables S3-S4).<sup>[17]</sup> The dominating graphitic N and pyridinic N can greatly promote the oxygen catalytic

performance, because they are responsible for conductivity and activity, respectively.<sup>[18]</sup> The electronic conductivities of the different solid powder were obtained through the four-point probe test (**Figure S5a**). Compared with the conductivity of GNs ( $0.9 \text{ S cm}^{-1}$ ), the conductivity of Fe-N/G-Co increases sharply to  $6.5 \text{ S cm}^{-1}$ , which is even better than those of Pt/C ( $5.6 \text{ S cm}^{-1}$ ) and RuO<sub>2</sub> ( $4.9 \text{ S cm}^{-1}$ ).<sup>[19]</sup> This result proves that the doping of metal and nitrogen can improve the conductivity of the carbon matrix.

## 2.2. Atomic Structure Analysis of Fe-N/G-Co

The structure of Fe-N/G-Co, Fe-N/G and N/G-Co at the atomic scale is further revealed by high angle annular dark field (HAADF) imaging with aberration-corrected scanning TEM (STEM). As shown in **Figure 2a-c**, numerous individual brighter spots representing heavy metal atoms can be clearly identified as isolated single metal atoms throughout the graphene matrix.<sup>[20]</sup> Energy disperse spectroscopy (EDS) elemental mapping was further performed under the STEM mode, which demonstrates that Fe, Co, C, N, and O elements are homogeneously distributed on the Fe-N/G-Co sample (**Figure S6**).

To further investigate the chemical state and local coordination structure of metal atoms in Fe-N/G-Co, Fe-N/G and N/G-Co, X-ray absorption near edge structure (XANES) and extended X-ray fine structure (EXAFS) spectroscopy measurements were employed (Figure 2d-i). These results are shown along with those reference sample Fe-foil, Fe<sub>2</sub>O<sub>3</sub>, FePc, Co-foil, CoO, and CoPc.<sup>[12]</sup> As shown in Figure 2d&g, the XANES profiles of Fe-N/G-Co, Fe-N/G and N/G-Co show significant difference from those of the reference samples. The Fe K-edge WL intensities are in an increasing order of Fe foil < Fe-N/G-Co < FePc < Fe-N/G < Fe<sub>2</sub>O<sub>3</sub>, while the Co K-edge WL intensities are in an increasing order of Co foil < CoPc < N/G-Co < Fe-N/G-Co < CoO. Noticeably, the number of unoccupied electron density states of Fe sites in Fe-N/G-Co is decreased compared with Fe-N/G while that of Co sites in Fe-N/G-Co is increased compared with N/G-Co, respectively.<sup>[11b]</sup> These results illustrate that electron transfer can take place

between Fe and Co for Fe-N/G-Co, which may trigger synergistic effect to accelerate the charge transfer and improve the catalytic activity.<sup>[21]</sup>

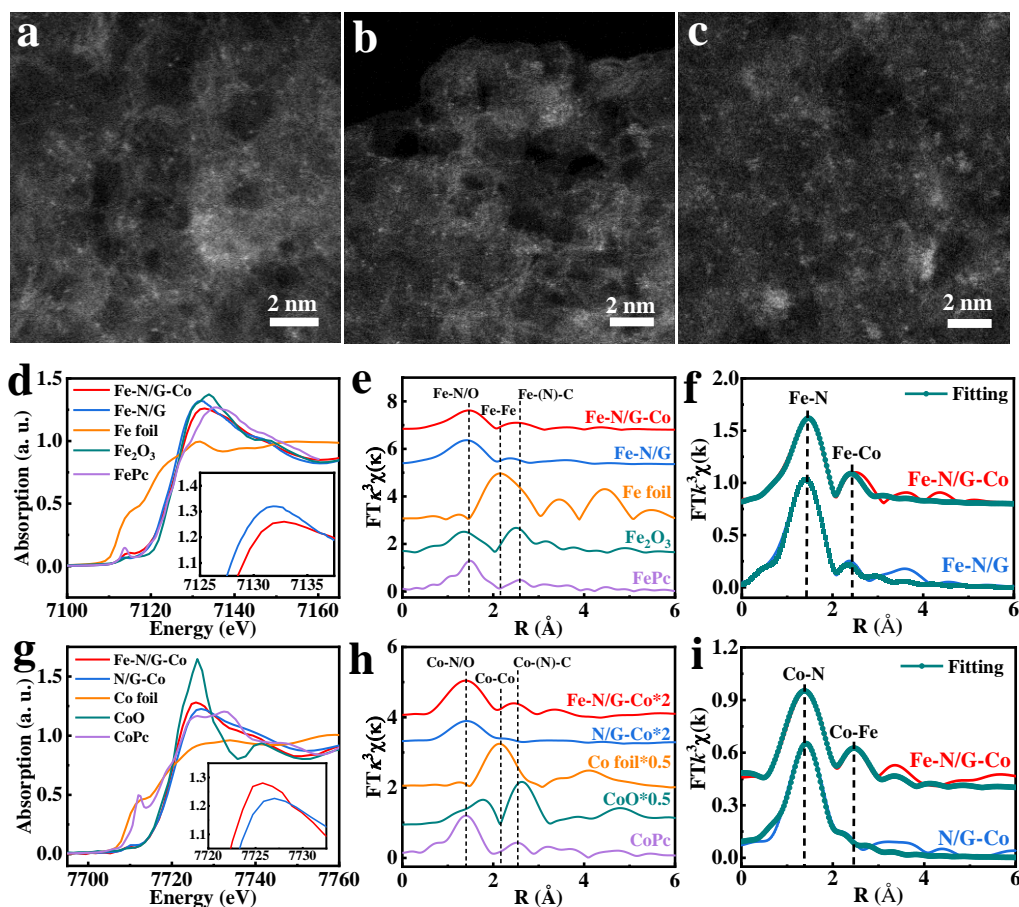


**Figure 2.** Structure characterizations of Fe-N/G-Co, Fe-N/G and N/G-Co. (a-c) Atomic-resolution HAADF-STEM image of the Fe-N/G-Co, Fe-N/G and N/G-Co samples. (d) XANES and (e) Fourier transforms of EXAFS spectra of Fe-N/G-Co, Fe-N/G and references at Fe K-edge. (f) The EXAFS fitting in R space for Fe-N/G-Co and Fe-N/G. (g) XANES and (h) Fourier transforms of EXAFS spectra of Fe-N/G-Co, N/G-Co and references at Co K-edge. (i) The EXAFS fitting in R space for Fe-N/G-Co and N/G-Co.

The coordination environments of Fe and Co atoms in Fe-N/G-Co, Fe-N/G and N/G-Co were further elucidated by Fourier transformations (FT) of  $k^3$ -weighted for EXAFS (FT-EXAFS).<sup>[22]</sup> As shown in Figure 2e, the main peaks in Fe-N/G-Co and Fe-N/G observed around 1.47 Å are associated with Fe-N/O bonds and no Fe-Fe (ca. 2.15 Å) contribution is found. These results exclude the existence of Fe nanoparticles, consistent with the observation of HAADF-STEM images. Similarly, metallic bonds of cobalt (ca. 2.15 Å) are absent from Fe-N/G-Co and N/G-Co (Figure 2h). The FT-EXAFS curves were fitted in R space to obtain the coordination

environment of Fe in Fe-N/G-Co and Fe-N/G and that of Co in Fe-N/G-Co and N/G-Co (Figure 2f&i and Tables S5-S6).<sup>[21]</sup> In addition to Fe-N (1.99 Å, 4.1) and Co-N (2.00 Å, 3.8) bonds, there is also the contribution of Fe-Co (2.69 Å, 1.3) bonds in Fe-N/G-Co, which is different from the results of Fe-N/G and N/G-Co. Combining the XAS analyses with the HADDF-STEM results, it is confirmed that Fe and Co in Fe-N/G-Co exist in the form of single atoms, which are coordinated with nitrogen atoms and interact with each other.

### 2.3. Electrochemical properties

Electrochemical evaluation was carried out to probe the bifunctional oxygen electrocatalytic performance of Fe-N/G-Co, Fe-N/G and N/G-Co single-atom catalysts. Commercial 20 wt% Pt/C and RuO<sub>2</sub> were selected as the benchmark ORR and OER electrocatalysts, respectively. All electrochemical measurements were performed in oxygen-saturated 0.10 M KOH aqueous electrolyte at room temperature with an areal loading of 0.10 mg cm<sup>-2</sup> for all electrocatalysts. All the polarized profiles were referenced to the reversible hydrogen electrode (RHE) and calibrated with 95% iR-compensation (Figure S5b).

The ORR activity of the pristine N-doped GNs and various metal doped samples were evaluated using linear sweep voltammetry (LSV) (**Figure 3a-b**). The half-wave potential ( $E_{1/2}$ ) and Tafel slope have the following relationship: N/G (0.79 V, 72.5 mV dec<sup>-1</sup>) < N/G-Co (0.80 V, 72.5 mV dec<sup>-1</sup>) < Fe-N/G (0.83 V, 70.1 mV dec<sup>-1</sup>) < Fe-N/G-Co (0.85 V, 69.8 mV dec<sup>-1</sup>), inferring that the doping of Fe and Co metal atoms can increase the catalytic activity of ORR, and the dual-metal doping can further reduce the energy barrier. Fe-N/G-Co delivers the same  $E_{1/2}$  to that of Pt/C (0.85 V) (Figure 3a). As the Tafel slope is a critical factor to evaluate the reaction kinetics of catalysts, Figure 3b manifests that the ORR kinetics is significantly improved on the Fe-N/G-Co electrocatalyst (69.8 mV dec<sup>-1</sup>) over Pt/C (72.6 mV dec<sup>-1</sup>).<sup>[9b]</sup> As shown in the CV curve of **Figure S7**, Fe-N/G-Co exhibits a quasi-rectangular double-layer capacitance current in N<sub>2</sub>-saturated 0.1M KOH, and a strong cathodic reduction peak appears

after replacing N<sub>2</sub> with O<sub>2</sub>. It stems from fine mass transfer ability and abundant active sites, which are consistent with TEM and BET results.

The ORR catalytic selectivity was evaluated by the Koutecky-Levich (K-L) equations and rotating ring disk electrode (RRDE) measurements as shown in Figure 3c-d. The ORR electron transfer number (*n*) of Fe-N/G-Co is 3.79-3.97 in the potential range 0-0.8 V versus RHE, corresponding to a low H<sub>2</sub>O<sub>2</sub> yield of 10.68-1.35%, indicating the dominant 4e<sup>-</sup> ORR process similar to the Pt/C (3.66-3.96) electrocatalyst. In comparison, the *n* value is 3.70-3.88 and 3.69-3.87 for the Fe-N/G and N/G-Co, respectively, implying the Fe-N/G-Co is easier to access to the desirable 4e<sup>-</sup> ORR process.<sup>[23]</sup> Thus, the Fe-N/G-Co exhibits the highest E<sub>1/2</sub> (0.85 V) and electron transfer number (~3.80), and the smallest Tafel slope (69.8 mV dec<sup>-1</sup>), proving that the multi-metal doping strategy can change the electronic structure and trigger the synergistic effect between Fe-N<sub>x</sub>/C and Co-N<sub>x</sub>/C to accelerate charge transfer and improve the catalytic activity.

The long-term stabilities of Fe-N/G-Co and 20 wt% Pt/C were measured by extended electrolysis including cyclic voltammetry (CV) curves and chronoamperometry (CA) curves.<sup>[24]</sup> As shown in Figure 3e, after 10000 cycles between 0.1 and 0.9 V vs. RHE in O<sub>2</sub>-saturated 0.1 M KOH, the E<sub>1/2</sub> of Fe-N/G-Co shows only 5 mV vs. RHE decay. In comparison, the decay of E<sub>1/2</sub> of the Pt/C was tested to be 37 mV vs. RHE after 10000 cycles (**Figure S8a**), indicating the good durability of Fe-N/G-Co. CA curve shows that Fe-N/G-Co retains 93.4% current after 50 h test in O<sub>2</sub>-saturated electrolyte (Figure 3e, inset), which also outperforms that of the Pt/C catalyst (remaining 80.2% in current density). Moreover, to evaluate the methanol-crossover effect of Fe-N/G-Co, 60 mL methanol was added to 180 mL O<sub>2</sub>-saturated 0.1 M KOH electrolyte solution at the potential of 0.6 V vs. RHE (Figure 3f). As a result, the current density of Pt/C immediately showed a sharp drop with the addition of methanol, which may be caused by the sharp drop in the pH of the electrolyte.<sup>[25]</sup> In contrast, the current density of the Fe-N/G-Co catalyst even stepped up and then slowly dropped, proving that Fe-N/G-Co is not sensitive to methanol, making it a promising candidate for methanol fuel cells.<sup>[2c]</sup>

The OER reactivity and kinetics are similarly evaluated according to LSV profiles and Tafel slopes but with RuO<sub>2</sub> as the reference electrocatalyst. The OER overpotential required to reach the current density of 10 mA cm<sup>-2</sup> ( $\eta_{10}$ ) is selected as the descriptor for OER reactivity. The  $\eta_{10}$  value and Tafel slope of Fe-N/G-Co are 440 mV and 76.4 mV dec<sup>-1</sup>, which is significantly better than those of N/G-Co (500 mV, 204.1 mV dec<sup>-1</sup>), Fe-N/G (510 mV, 162.7 mV dec<sup>-1</sup>) and original N/Gs (670 mV, 213.8 mV dec<sup>-1</sup>) (Figure 3g-h), indicating inferior OER reactivity of the Fe-N/G-Co electrocatalyst. Though the activity of Fe-N/G-Co is slightly lower than that of RuO<sub>2</sub> ( $\eta_{10}$ , 410 mV), but its Tafel slope (76.4 mV dec<sup>-1</sup>) is lower than that of RuO<sub>2</sub> (98.2 mV dec<sup>-1</sup>), indicating that the OER reaction kinetics of Fe-N/G-Co is faster, and this advantage is especially evident at high current density. In addition, Fe-N/G-Co also demonstrates impressive electrochemical stability, maintaining a current density of 82.4% during a 10-hour CA test at 1.6 V in O<sub>2</sub>-saturated 0.1M KOH, much higher than the 15.8% of RuO<sub>2</sub> (Figure S8b). The stability of Fe-N/G-Co catalyst is probably ascribed to the well-designed stable structure of single-atom active site and the highly graphitized carbon substrate.<sup>[1b]</sup>

The high specific surface area and atomic level dispersion of Fe-N/G-Co, Fe-N/G and N/G-Co increase the electrochemical surface area (ECSA) (**Figure S9** and Table S7), which is advantageous for oxygen electrocatalysis.<sup>[26]</sup> Even if the mass content of Pt and Ru is much higher than that of Fe-N/G-Co, the electrocatalytic performance of Pt/C and RuO<sub>2</sub> electrocatalysts is far from satisfactory, due to limited ECSA (**Figure S10**). Last, the performances of Fe-N/G-Co are compared with other currently reported non-noble metal single-atom bifunctional oxygen electrocatalysts in terms of the catalyst loading amount and the potential gap ( $\Delta E$ ) between the ORR  $E_{1/2}$  and the OER  $\eta_{10}$ , which is crucial to the practical application of Zn-air batteries (Figure 3i, Figure S8c and Table S8).<sup>[9b,27]</sup> At a low areal loading of 0.10 mg cm<sup>-2</sup>, the  $\Delta E$  of Fe-N/G-Co electrocatalyst is 0.82 V, which is better than other reported catalysts. Based on these analyses, it can be determined that Fe-N/G-Co electrocatalyst indeed shows superior bifunctional oxygen catalytic performance.

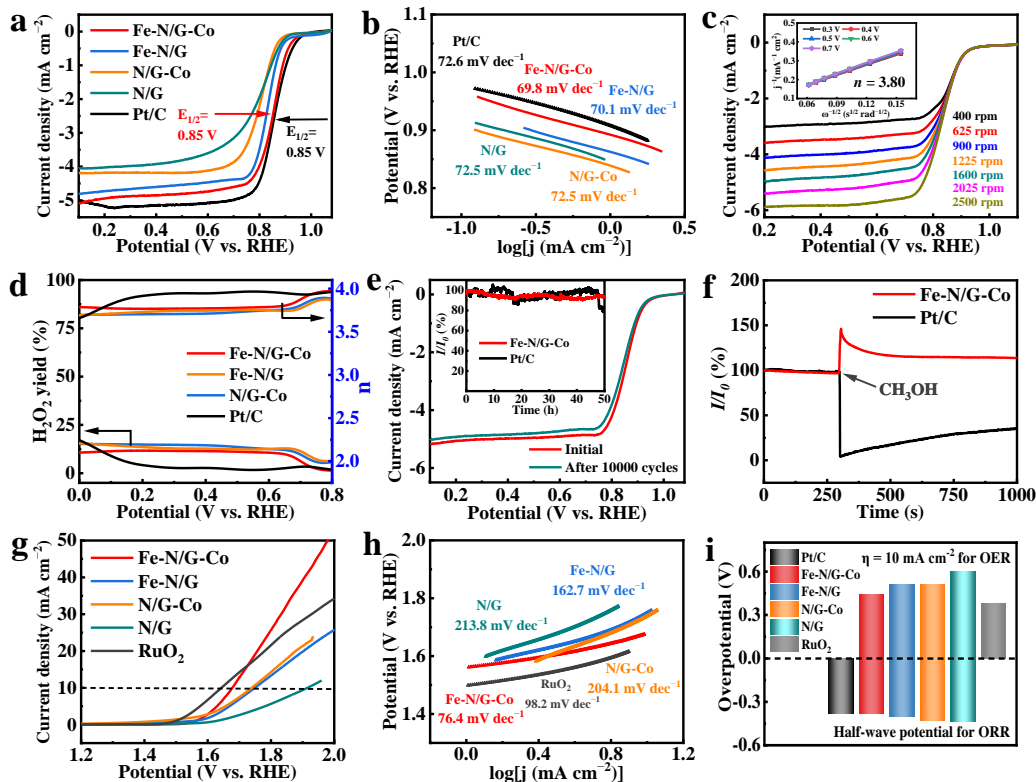


**Figure 3.** Bifunctional oxygen electrocatalytic performance evaluation of the dual-metal single-atom Fe-N/G-Co, Fe-N/G, N/G-Co and reference electrocatalysts. (a) The ORR polarization curves of all samples in 0.1 M KOH solution. (b) Tafel plots for ORR. (c) ORR polarization curves of Fe-N/G-Co at different rotating rates (inset: K-L plots and electron transfer numbers). (d)  $\text{H}_2\text{O}_2$  yield and corresponding electron transfer number calculated by using RRDE method. (e) ORR polarization plots of Fe-N/G-Co catalyst before and after 10000 potential cycles, inset shows the  $i$ - $t$  curve at 0.8 V for 50 h. (f) Chronoamperometric response of Fe-N/G-Co and Pt/C at 0.6 V in  $\text{O}_2$  saturated 0.1 M KOH with the addition of methanol. (g) The OER polarization curves of all samples in 0.1 M KOH solution. (h) Tafel plots for OER. (i) Comparison of ORR/OER bifunctional electrocatalytic performance of Fe-N/G-Co, Fe-N/G, N/G-Co, N/G, Pt/C and  $\text{RuO}_2$ .

The successful construction of dual-metal single-atom Fe-N/G-Co catalyst and its outstanding bifunctional oxygen electrocatalytic performance promise the further application in Zn-air batteries. Conventional or novel flexible rechargeable Zn-air batteries are composed of a zinc foil as the anode, alkaline electrolyte, and an air cathode where the oxygen redox reactions take place.<sup>[28]</sup> The cathode reactions constitute the bottleneck of Zn-air batteries because of sluggish kinetics of both ORR and OER. Therefore, the single-atom Fe-N/G-Co electrocatalyst was loaded on conductive carbon paper to construct the air cathode for better battery performance. Noble-metal-based Pt/C+ $\text{RuO}_2$  cathode was also prepared by the same

procedures as the reference cathode. The areal loading of both the electrocatalysts is  $1.0 \text{ mg cm}^{-2}$ .

As depicted in **Figure 4a** and **Figure S11a**, the open-circuit voltage (OCV) of the Fe-N/G-Co cathode ( $1.54 \text{ V}$ ) was close to the theoretical value of  $1.65 \text{ V}$  and higher than that of Pt/C+RuO<sub>2</sub> cathode ( $1.42 \text{ V}$ ). The rate performance was evaluated by discharging at different current densities. As indicated in Figure 4b, the Fe-N/G-Co cathode exhibits discharge voltages of  $1.29$ ,  $1.26$ ,  $1.23$ , and  $1.13 \text{ V}$  at the current density of  $2$ ,  $5$ ,  $10$  and  $25 \text{ mA cm}^{-2}$ , respectively, which are much higher than those of Pt/C+RuO<sub>2</sub> cathode. The voltage value can be recovered as the current density decreases again. LSV was performed to evaluate the reactivity of the cathode reactions. Correspondingly, a peak discharge power density of  $98.8 \text{ mW cm}^{-2}$  was achieved on the Fe-N/G-Co cathode, which is much higher than that of Pt/C+RuO<sub>2</sub> cathode ( $42.1 \text{ mW cm}^{-2}$ ) (Figure 4c). Superior LSV performance of the Fe-N/G-Co cathode suggests improved ORR kinetics and electrocatalytic capability in agreement with the rate performance.

When normalized to the mass of consumed Zn, the Zn-air battery based on Fe-N/G-Co electrocatalyst delivered a specific capacity and energy of  $808.9 \text{ mAh g}_{\text{Zn}}^{-1}$  and  $952.8 \text{ Wh kg}_{\text{Zn}}^{-1}$  at  $10 \text{ mA cm}^{-2}$ , corresponding to  $98.6\%$  and  $70.6\%$  utilization of the theoretical values ( $820.0 \text{ mAh g}_{\text{Zn}}^{-1}$ ,  $1349.3 \text{ Wh kg}_{\text{Zn}}^{-1}$ ), superior to those of Pt/C+RuO<sub>2</sub> ( $752.1 \text{ mAh g}_{\text{Zn}}^{-1}$ ,  $774.8 \text{ Wh kg}_{\text{Zn}}^{-1}$ ) (Figure 4d). These values from Fe-N/G-Co-based Zn-air battery are competitive with many reported air-cathodes (Table S9). The stability of the cathodes was characterized using long-term cycling tests. The Fe-N/G-Co cathode exhibits an initial discharge/charge voltage gap of  $1.25 \text{ V}$  at  $10.0 \text{ mA cm}^{-2}$ , while Pt/C+RuO<sub>2</sub> cathode exhibits  $1.31 \text{ V}$  (Figure 4e and Figure S11b). The Fe-N/G-Co cathode affords 225 cycles corresponding to 112.5 h, which is much better than Pt/C+RuO<sub>2</sub> cathode (160 cycles, 80 h). Therefore, the dual-metal single-atom Fe-N/G-Co cathode with outstanding bifunctional oxygen electrocatalytic performance demonstrates promising reactivity and stability in Zn-air batteries, suggesting the great potential

of Fe-N/G-Co to replace the noble metal-based catalysts in practical applications of Zn-air batteries.

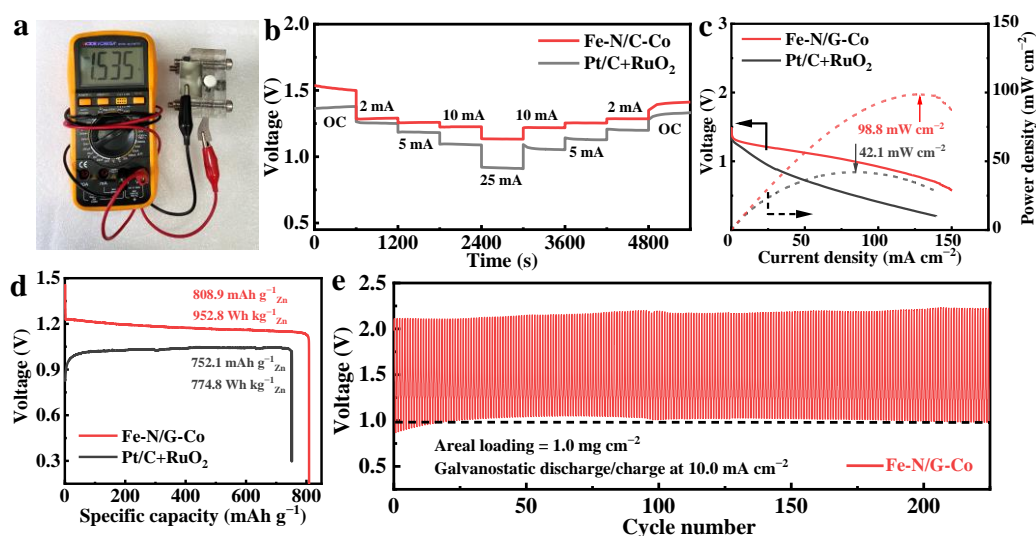


**Figure 4.** Electrochemical evaluation of the single-atom Fe-N/G-Co-based cathode in rechargeable Zn-air batteries. (a) Photograph of the Zn-air battery with an open-circuit voltage of 1.535 V. (b) Discharge profiles at the different current densities (open-circuit voltage (OCV), 1.0, 2.0, 5.0, 10.0, and 25 mA cm<sup>-2</sup>, and recovery to OCV. (c) Discharge polarization curves and corresponding power density plots of the Zn-air batteries using Fe-N/G-Co and Pt/C+RuO<sub>2</sub> as air electrode, respectively. (d) Discharge curves at a constant current density of 10 mA cm<sup>-2</sup>. (e) The discharge and charge voltage profiles of Zn-air batteries with Fe-N/G-Co at 10 mA cm<sup>-2</sup>.

## 2.4. Theoretical calculations

To investigate the binding energy and evolution process of oxygen-containing intermediates at individual and dual-metal single-atom active sites, we constructed simplified and thermodynamically stable models: Fe-N<sub>4</sub>/C, Co-N<sub>4</sub>/C and FeCoN<sub>6</sub>OC, which can be seen in **Figure S12**. Fe-N<sub>4</sub>/C and Co-N<sub>4</sub>/C are typical metal-N<sub>4</sub>/graphene structures, while in FeCoN<sub>6</sub>OC, Fe atom and Co atom are coordinated by three nitrogen atoms respectively and bridged by an oxygen atom, labeled as Fe-Co dual-site.

Then we studied the processes of ORR and OER on above three simplified models. Note that ORR/OER intermediates are more easily adsorbed on the Fe site than Co site, so ORR and OER mainly occur on the Fe site for FeCoN<sub>6</sub>OC. **Figure 5a** delivers the optimized structures of various intermediates along the reaction path at the N<sub>3</sub>Fe-O-CoN<sub>3</sub> dual-site. The similar reaction schemes for Fe-N<sub>4</sub>/C and Co-N<sub>4</sub>/C can be found in **Figure S13**. The free energy

landscapes are summarized in **Figure S14** and the free energy barriers of critical reaction steps are marked with corresponding colors. For ORR (Figure S14a), the adsorption of O<sub>2</sub> on the catalyst is energetically rather favorable, and it is not the rate-limiting step of ORR. All surfaces have the same rate-limiting step, that is, the formation of \*OOH. Ordered by the energy required for the formation of \*OOH, the sequence of the ORR activity at three catalysts is: FeCoN<sub>6</sub>OC > Fe-N<sub>4</sub>/C > Co-N<sub>4</sub>/C, which is consistent with our experimental results. As for OER (Figure S14b), the reaction activity is determined by the rate-limiting step of four electron steps and the desorption of O<sub>2</sub>. Thanks to the lower barrier of the rate-controlled step reaction, the OER activity of Co-N<sub>4</sub>/C is higher than that of Fe-N<sub>4</sub>/C. Inspiringly, after the introduction of additional Co atoms at the Fe-N<sub>x</sub>/C site, the formation energy of \*OOH and the desorption energy of O<sub>2</sub> are greatly reduced, which accounts for the high OER activity of FeCoN<sub>6</sub>OC.

Further, to explain why FeCoN<sub>6</sub>OC has the highest ORR and OER activity, a projected density of states (PDOS) analysis of metal(d)-involved orbital was performed by using VASPKIT, and a PDOS plot is shown in Figure S14c.<sup>[29]</sup> As shown, Fe-N<sub>4</sub>/C has a very rich PDOS distribution not far above the Fermi level, while Co-N<sub>4</sub>/C has less PDOS distribution above the Fermi level, which means that the Fe's unoccupied orbitals are more prone to accept electrons from the lone electron pair of oxygen. As a consequence, Fe-N<sub>4</sub>/C has a stronger interaction with the ORR/OER intermediates than Co-N<sub>4</sub>/C. As for FeCoN<sub>6</sub>OC, on the one hand, the special coordination environment makes the distribution of Fe(d)-involved orbital very diffuse, causing a weaker interaction with the ORR/OER intermediates than Fe-N<sub>4</sub>/C. On the other hand, for \*OH and \*OOH, a significant hydrogen bond interaction enhances the adsorption of OH and OOH on FeCoN<sub>6</sub>OC. In a word, hydrogen bond interaction and moderate adsorbate-metal interaction make ORR and OER much more energetically favorable.

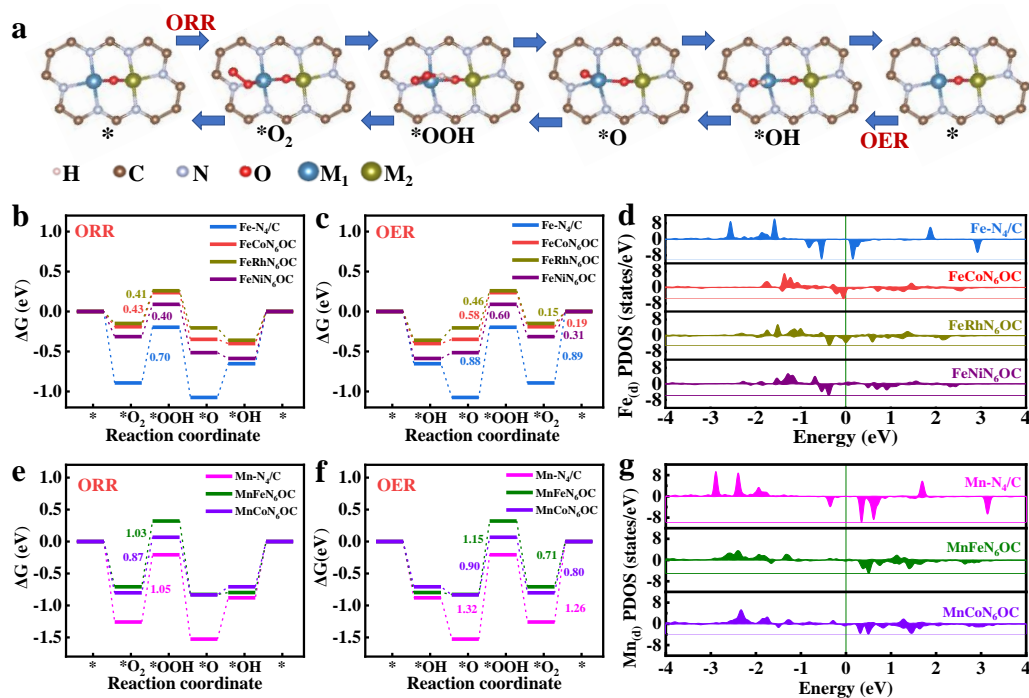


**Figure 5.** (a) Proposed reaction scheme on  $M_1M_2N_6OC$  ( $M_1 = Fe, Mn$ ;  $M_2 = Co, Rh, Ni, Fe$ ). (b, e) The free energy landscapes of ORR on different catalysts at 1.23 V. (c, f) The free energy landscapes of OER on different catalysts at 1.23 V. (d, g) The projected density of states (PDOS) of Fe or Mn(d)-involved orbital. The Fermi level is set as the energy zero point.

## 2.5. Outlook-Extension to Other Catalysts

We are also very interested in whether this bimetal strategy works well with other metal combinations. An extended DFT study was performed to construct individual and dual-metal single-atom active sites,  $M_1-N_4/C$ ,  $M_2-N_4/C$  and  $M_1M_2N_6OC$  ( $M_1 = Fe, Mn$ ;  $M_2 = Co, Rh, Ni, Fe$ ), consistent with the above models. The free energy change ( $\Delta G$ ) of oxygen-containing intermediates at the  $M-N_4/C$  site was systematically studied (Figure S15a). Ordered by  $G(*OH)$ ,  $G(*O)$ ,  $G(*OOH)$  and  $G(*O_2)$ , the sequence of the adsorption strength of the intermediates at these single metal sites is:  $Mn-N_4/C > Fe-N_4/C > Co-N_4/C > Rh-N_4/C > Ni-N_4/C$ . For ORR, all single metal sites have same rate-limiting step, i.e.  $*OOH$  formation (Figure S15b). The formation energy of  $*OOH$  ( $G(*OOH) - G(*O_2)$ ) is much higher than that of other steps and hence disfavor ORR. As for OER, the adsorption strength of  $*O$  intermediate is essential (Figure S15c). In particular, the strong adsorption simultaneously brings high  $*OOH$  formation energy ( $G(*OOH) - G(*O)$ ), while the weak adsorption is accompanied by high  $*O$  formation

energy ( $G(*O) - G(*OH)$ ). In addition, strong adsorption sites, i.e. Mn-N<sub>4</sub>/C and Fe-N<sub>4</sub>/C, have higher O<sub>2</sub> desorption energy. Hence, single metal sites cannot show excellent ORR/OER performance.

Interestingly, although traditional Fe-N<sub>4</sub>/C and Mn-N<sub>4</sub>/C single metal sites have too strong adsorption energy for ORR/OER intermediates, resulting in poor oxygen catalytic performance, after the introduction of a heterogenous metal, the energy barrier of the key rate-limiting step of ORR/OER on Fe and Mn sites is significantly reduced (Figure 5b-c and Figure 5e-f). This is because the bimetal strategy adjusts the d-band distribution of Fe and Mn and reduces the adsorption energy of ORR/OER intermediates (Figure 5d&g). At the same time, the hydrogen bond interaction stabilizes the adsorption state of \*OH and \*OOH to a certain extent, resulting in lower formation energies of \*OH and \*OOH. As a result, bimetallic sites have significantly enhanced performance in both OER and ORR than single-metallic sites.

In order to further investigate the general applicability of this strategy and exclude the influence of active site density, Co-N/G-Co, Mn-N/G, Mn-N/G-Fe and Mn-N/G-Co samples were prepared. As shown in **Figures S16-S17**, Co and Mn atoms in Co-N/G-Co and Mn-N/G-Co are uniformly dispersed on the surface of the carbon substrate. The performance difference between Co-N/G-Co and Co-N/G (**Figure S18**) indicates that the change of active site density has an effect on the limiting current density, but has a small impact on the overpotential and Tafel slope. Notably, Fe-Co, Mn-Fe and Mn-Co dual-metal sites in Fe-N/G-Co, Mn-N/G-Fe and Mn-N/G-Co catalysts not only increase the ORR/OER limiting current density, but also reduce the overpotential and Tafel slope, proving the successful construction of the synergistic effect (Figure 3 and **Figures S19-S20**).

### 3. Conclusion

In summary, a novel chelating-adsorbing method is proposed to fabricate dual-metal single-atom M<sub>1</sub>-N/G-M<sub>2</sub> (M<sub>1</sub> = Fe, Mn; M<sub>2</sub> = Co, Rh, Ni, Fe) electrocatalysts. Experimental and theoretical results proved that the introduction of a heterogenous metal can regulate the

electronic structure of the single-atom active site, optimize the adsorption energy of the intermediate, and trigger a synergistic effect, thereby improving the performance of ORR/OER and rechargeable Zn-air batteries. The improved performance of Fe-N/G-Co D-SAC is mainly derived from three aspects: (1) the huge surface area yielding highly dispersed active sites and ideal electrochemical surface area; (2) the modulation of Fe-N<sub>x</sub>/C electronic structure by Co-N<sub>x</sub>/C; and (3) the high degree of graphitization of the carbon material, resulting in increased electrical conductivity and chemical stability. The findings of this work not only clearly indicate the unique synergistic effect in bimetal-doped catalysts, but also provide a new strategy to tailor the electronic structure of single-atom sites.

## **4. Materials and Methods**

### **4.1. Reagents**

Iron(III) nitrate nonahydrate [Fe(NO<sub>3</sub>)<sub>3</sub>·9H<sub>2</sub>O, 99%], manganese acetate tetrahydrate [Mn(CH<sub>3</sub>COO)<sub>2</sub>·4H<sub>2</sub>O, 99%], ethylenediaminetetraacetic acid disodium salt (EDTA-2Na, 99.8%), melamine (99%), sodium chloride (NaCl), potassium chloride (KCl), and absolute ethanol (CH<sub>3</sub>CH<sub>2</sub>OH) and H<sub>2</sub>SO<sub>4</sub> (GR) were obtained from Shanghai Chemical Reagents, China. Nafion (5 wt% in a mixture of lower aliphatic alcohol and water) were acquired from Sigma-Aldrich. Cobalt(II) nitric acid hexahydrate [Co(NO<sub>3</sub>)<sub>2</sub>·6H<sub>2</sub>O, 99.99%], hydrogen peroxide (30%) and potassium hydroxide were obtained from Shanghai Aladdin Bio-Chem Technology Co., LTD. Zinc acetate dihydrate [Zn(CH<sub>3</sub>COO)<sub>2</sub>·2H<sub>2</sub>O, 99.99%] was acquired from Rhawn. Platinum on carbon (Pt/C, 20 wt%) was acquired from Sunlaite. Ruthenium oxide (RuO<sub>2</sub>, 99.9%) was acquired from Macklin. Deionized (DI) water (18.2 MΩ at 25°C) obtained from Milli-Q System (Millipore, Billerica, MA) was used for all our experiments. All chemical reagents were used as received without further purification.

### **4.2. Synthesis of Fe-N/G-Co**

In the first doping step, 5 g EDTA-2Na, 1.87g melamine and 0.5 mmol Fe(NO<sub>3</sub>)<sub>3</sub>·9H<sub>2</sub>O were initially dissolved into 200 mL deionized water, and then continuously stirred at 80°C for 12

hours. Subsequently, the solution was evaporated by rotation and transferred into a solid powder of Fe-EDTA-melamine. The as-obtained powder was then thoroughly mixed with 11.5 g NaCl and 13.5 g KCl powder through grinding within an agate mortar. The mixed precursors were placed in a corundum boat and annealed at 800°C for 1 h with a heating rate of 3°C·min<sup>-1</sup> under N<sub>2</sub> atmosphere. After naturally cooled down to room temperature, the black powder was washed with DI water through vacuum infiltration to remove NaCl and KCl completely. Then, the precipitant was vacuum dried at 60°C for 12h. Then the black sample was treated by acid leaching in 0.5 M H<sub>2</sub>SO<sub>4</sub> solution at 80°C for 6 h. Typically, 100 ml acid solution was used for 100 mg sample. Such prepared carbon samples labelled as p-Fe-N/G are ready for the second adsorption step.

In the second adsorption step, 100 mg p-Fe-N/G powder was dispersed into 50 mL water. 200 mg Co(NO<sub>3</sub>)<sub>2</sub>·6H<sub>2</sub>O and 400 μL 30 wt% H<sub>2</sub>O<sub>2</sub> solution dissolved in 20 mL H<sub>2</sub>O were added into the above suspensions, respectively. After ultrasound disperses for 0.5 h and moderate stirring for 10 h at room temperature, the resultant product was washed with DI water through vacuum infiltration and collected after drying. The final Fe-N/G-Co product was obtained after a heat treatment at 900°C under N<sub>2</sub> flow for 3 h.

N/G, M<sub>1</sub>-N<sub>4</sub>/C, M<sub>2</sub>-N<sub>4</sub>/C and M<sub>1</sub>M<sub>2</sub>N<sub>6</sub>OC (M<sub>1</sub> = Fe, Mn; M<sub>2</sub> = Co, Fe) were prepared by the same procedure but changing the metal precursor with or without the second adsorption step.

### **4.3. Material characterization**

X-ray diffractions (XRD) were recorded through an X'Pert PRO (PANalytical, Netherlands) instrument with Cu K radiation over the 2θ range from 10° to 80°. Raman spectroscopy was measured using using a Laser Confocal Raman Microspectroscopy (LabRAM HR Evolution, Horiba Jobin Yvon). Specific surface area and pore size distribution were measured by using nitrogen adsorption/desorption isotherms through the Brunauer-Emmett-Teller (BET, AUTOSORB-IQ2-MP) method at 77 K. BJH method is selected to calculate the pore-size

distribution. X-ray photoelectron spectroscopy (XPS) analyses were conducted with an Escalab 250Xi XPS system with Al K $\alpha$  (1486.6 eV) source. The amounts of metal loading in Fe-N/G-Co were determined by inductively coupled plasma-atomic emission spectroscopy (ICP-AES, ICAP7400). The resistance of the powder was measured by a four-point probe (ST2722). Scanning electron microscopy (SEM) was performed with a Hitachi S-4800 field-emission scanning electron microscope (FE-SEM) (5 kV). High-angle annular dark-field scanning transmission electron microscopy (HAADF-STEM) images were obtained on an FEI Titan ChemiSTEM equipped with a CEOS (Heidelberg, Germany) probe corrector, operating at 200 kV. Transmission electron microscopy (TEM) and high-resolution transmission electron microscopy (HRTEM) were conducted using a JEM-2100F field-emission TEM at an acceleration voltage of 200 kV equipped with an energy-dispersive X-ray spectroscope (EDS). Fe and Co K-edge X-ray absorption spectra were acquired at room temperature in fluorescence mode at beamline 7-BM at NSLS II using a channel cut Si (111) monochromator. The storage ring of NSLS II was operated with a current of 400 mA. Harmonic rejection was achieved by a detuning of 30%. The energy was calibrated using metal foils. Athena and Artemis codes were used to extract the data and fit the profiles.<sup>[30]</sup>

#### **4.4. Electrochemical tests**

**Oxygen Reduction Measurements.** All electrochemical measurements were conducted in a conventional three-electrode cell at room temperature ( $\sim 25^\circ\text{C}$ ) using the 760E Bipotentiostat (CH Instruments). Catalyst ink was prepared by ultrasonically dispersing 2 mg of Fe-N/G-Co catalyst or Pt/C catalyst (20 wt% Pt) in a suspension containing 50  $\mu\text{L}$  Nafion (5 wt%) solution and 950  $\mu\text{L}$  ethanol. The catalyst film coated electrode was obtained by dispersing the catalyst ink on a glassy carbon rotating ring-disk electrode followed by drying in air. The catalyst loadings on RRDE were  $0.10 \text{ mg cm}^{-2}$  for Fe-N/G-Co catalyst and Pt/C catalyst. The electrolyte

was 0.1 M KOH solution for ORR measurement. Onset potential is defined as the potential at which the ORR current is  $0.1 \text{ mA cm}^{-2}$ .

The ORR apparent number of electrons transferred, RRDE measurements, methanol-crossover effect and cyclic stability of catalysts were tested according to previously reported work.<sup>[31]</sup> Chronoamperometric (CA) measurements were conducted with the potential holding at 0.8 V vs. RHE O<sub>2</sub>-saturated 0.1 M KOH electrolyte.

**Oxygen Evolution Measurements.** The activity for the OER was subsequently tested by scanning between approximately 1.0 and 2.0 V in oxygen saturated 0.1 M KOH with a scan rate of  $10 \text{ mV s}^{-1}$  and the data were calibrated with 95% iR-compensation. Electrochemical impedance spectroscopy (EIS) measurements were made by applying an alternating voltage with an amplitude of 5 mV at frequencies ranging from  $10^6 \text{ Hz}$  to 0.1 Hz. CA measurements were conducted with the potential holding at 1.6 V O<sub>2</sub>-saturated 0.1 M KOH electrolyte at a rotating rate of 1600 rpm. Commercial RuO<sub>2</sub> catalyst were also measured at a loading of  $0.1 \text{ mg cm}^{-2}$  for comparison. In all figures, the potentials were converted to values versus the reversible hydrogen electrode (RHE).

**Zn-air Battery Measurements.** The Zn-air battery measurements were performed with a homemade Zn-air cell. The air cathode includes the hydrophobic carbon paper with a catalyst layer on the electrolyte-facing side and a gas-diffusion layer on the air-facing side. The catalyst ink was dropped and painted onto the carbon paper ( $1.0 \text{ cm}^2$ ) to fabricate the catalyst layer with a catalyst loading of  $1.0 \text{ mg cm}^{-2}$ . A polished zinc foil (0.2 mm thickness) was used as anode. Both electrodes were assembled into a Zn-air battery, and 6 M KOH aqueous solution with 0.2 M Zn(CH<sub>3</sub>COO)<sub>2</sub> was used as the electrolyte.

The linear scan voltammetry was performed in the open-circuit potential (OCP) to 0.2 V at a scan rate  $5 \text{ mV s}^{-1}$  to evaluate the current density and power density of the battery. The rate performance of Zn-air batteries was evaluated by galvanostatic discharge at a series of current

density of 2.0, 5.0, 10, 25, and back to 10, 5.0, and 2.0 mA cm<sup>-2</sup>. The specific capacity of Zn-air batteries was determined by the galvanostatic discharge profiles at 10 mA cm<sup>-2</sup>, which were then normalized to the mass of consumed Zn. The cycling stability test was carried out in a Land CT2001A system with 5 min rest time between each discharge and charge at a current density of 10 mA cm<sup>-2</sup>. Each discharge and charge period was set to be 10 min. The tests were operated in ambient air condition.

#### 4.5. Theory calculation

In this work, all DFT calculations were performed in the Vienna ab initio simulation package (VASP), Version 5.4.4.<sup>[32]</sup> The generalized gradient approximation (GGA) functional PBE,<sup>[33]</sup> the projector augmented wave (PAW) method and the 400 eV energy cutoff were adopted.<sup>[34]</sup> The van der Waals interaction was considered using the DFT-D3BJ correction.<sup>[35]</sup> For simplified catalyst models, A large supercell of (5×5) was modeled based on single layer graphite-(001) of symmetry P6mmm with  $\alpha=\beta=90^\circ$ ,  $\gamma=60^\circ$ . In addition, a vacuum space of 15 Å was employed to avoid the interaction between adjacent periodic units. Brillouin zone was sampled with a 3×3×1 k-points using a Gamma centered scheme grid for electronic self-consistent calculations, geometry optimizations and frequency calculations, while with a 5×5×1 k-points for density of states (DOS) calculations. For electronic self-consistent calculations and geometry optimizations, the convergence tolerance is set as follows: energy = $1.0\times 10^{-6}$ eV, force = $1.0\times 10^{-2}$  eV/Å. In addition, the calculation of thermal correction to Gibbs free energy and PDOS analysis were performed through the aid of VASPKIT, Version 1.2.1;<sup>[29]</sup> the visualization of periodic structures was carried out by VESTA, Version 3.5.5.<sup>[36]</sup>

#### Acknowledgements

The authors thank SSRF (beamline 11B) and National Synchrotron Light Source II (beamline 7-BM, QAS), a U.S. Department of Energy (DOE) Office of Science User Facility operated for the DOE Office of Science by Brookhaven National Laboratory under Contract No. DE-SC0012704 for the allocation of synchrotron beam time. This work was supported by National Key R&D Program of China (2018YFB0104300), the Leading Innovative and Entrepreneur Team Introduction Program of Zhejiang (2019R01006) and the 2019 Zhejiang University

Academic Award for Outstanding Doctoral Candidates (188310\*174222003/018/003). Thanks to Wikimedia Commons for the Ball & Stick models.

### Author Contributions

J. Ji and L. Wu contributed equally to this work. J. Ji and M. Ling conceived the idea and designed the experiments. J. Ji conducted the synthetic experiments and electrocatalytic tests. L. Wu and S.D. Zhou conducted the theoretical calculation. S.Y. Zhou, T. Qiu and Z. Li helped with characterization analysis. L. Wang, L. Ma and L. Zhang helped with synchrotron radiation testing. J. Ji, L. Wu, L. Wang, M. Ling, S.D. Zhou and C. Liang involved in the discussion of all results and wrote the manuscript.

### Conflicts of Interest

The authors declare that there is no conflict of interest regarding the publication of this article.

### Supporting Information

Supporting Information is available from the Wiley Online Library or from the author.

Received: ((will be filled in by the editorial staff))

Revised: ((will be filled in by the editorial staff))

Published online: ((will be filled in by the editorial staff))

### References

- [1] a) A. R. Zeradjanin, *Curr. Opin. Electroche.* **2018**, *9*, 214.; b) K. Zeng, X. Zheng, C. Li, J. Yan, J. H. Tian, C. Jin, P. Strasser, R. Yang, *Adv. Funct. Mater.* **2020**, *30*, 2000503.
- [2] a) Y. Li, H. Dai, *Chem. Soc. Rev.* **2014**, *43*, 5257.; b) J. Pan, Y. Y. Xu, H. Yang, Z. Dong, H. Liu, B. Y. Xia, *Adv. Sci.* **2018**, *5*, 1700691.; c) D. Chen, J. Ji, Z. Jiang, M. Ling, Z. Jiang, X. Peng, *J. Power Sources* **2020**, *450*, 227660.
- [3] S. Li, C. Cheng, X. Zhao, J. Schmidt, A. Thomas, *Angew. Chem. Int. Ed.* **2018**, *57*, 1856.
- [4] Y. Wang, H. Su, Y. He, L. Li, S. Zhu, H. Shen, P. Xie, X. Fu, G. Zhou, C. Feng, D. Zhao, F. Xiao, X. Zhu, Y. Zeng, M. Shao, S. Chen, G. Wu, J. Zeng, C. Wang, *Chem. Rev.* **2020**, *120*, 12217.
- [5] a) K. Liu, Y. Lei, G. Wang, *J. Chem. Phys.* **2013**, *139*, 204306.; b) I. Azcarate, C. Costentin, M. Robert, J. Savéant, *J. Am. Chem. Soc.* **2016**, *138*, 16639.; c) R. Gao, J. Wang, Z. Huang, R. Zhang, W. Wang, L. Pan, J. Zhang, W. Zhu, X. Zhang, C. Shi, J. Lim, J. Zou, *Nat. Energy* **2021**, *6*, 614-623.
- [6] X. Wang, Z. Chen, X. Zhao, T. Yao, W. Chen, R. You, C. Zhao, G. Wu, J. Wang, W. Huang, J. Yang, X. Hong, S. Wei, Y. Wu, Y. Li, *Angew. Chem. Int. Ed.* **2018**, *57*, 1944.
- [7] Y. Qu, B. Chen, Z. Li, X. Duan, L. Wang, Y. Lin, T. Yuan, F. Zhou, Y. Hu, Z. Yang, C. Zhao, J. Wang, C. Zhao, Y. Hu, G. Wu, Q. Zhang, Q. Xu, B. Liu, P. Gao, R. You, W. Huang, L. Zheng, L. Gu, Y. Wu, Y. Li, *J. Am. Chem. Soc.* **2019**, *141*, 4505.
- [8] Y. Yao, S. Hu, W. Chen, Z. Huang, W. Wei, T. Yao, R. Liu, K. Zang, X. Wang, G. Wu, W. Yuan, T. Yuan, B. Zhu, W. Liu, Z. Li, D. He, Z. Xue, Y. Wang, X. Zheng, J. Dong, C. Chang, Y. Chen, X. Hong, J. Luo, S. Wei, W. Li, P. Strasser, Y. Wu, Y. Li, *Nat. Catal.* **2019**, *2*, 304.
- [9] a) Y. Chen, S. Hu, F. Nichols, F. Bridges, S. Kan, T. He, Y. Zhang, S. Chen, *J. Mater. Chem. A* **2020**, *8*, 11649.; b) J. Chen, H. Li, C. Fan, Q. Meng, Y. Tang, X. Qiu, G. Fu, T. Ma, *Adv. Mater.* **2020**, *32*, 2003134.; c) X. Han, X. Ling, D. Yu, D. Xie, L. Li, S. Peng, C. Zhong, N. Zhao, Y. Deng, W. Hu, *Adv. Mater.* **2019**, *31*, 1905622.
- [10] Z. Liu, G. Zhang, Z. Lu, X. Jin, Z. Chang, X. Sun, *Nano Res.* **2013**, *6*, 293.
- [11] a) J. Wu, H. Zhou, Q. Li, M. Chen, J. Wan, N. Zhang, L. Xiong, S. Li, B. Y. Xia, G. Feng, M. Liu, L. Huang, *Adv. Energy Mater.* **2019**, *9*, 1900149.; b) J. Ji, Y. Sha, Z. Li, X. Gao, T. Zhang, S. Zhou, T. Qiu, S. Zhou, L. Zhang, M. Ling, Y. Hou, C. Liang, *Research* **2020**, *2020*, 1.
- [12] J. Li, M. Chen, D. A. Cullen, S. Hwang, M. Wang, B. Li, K. Liu, S. Karakalos, M. Lucero, H. Zhang, C. Lei, H. Xu, G. E. Sterbinsky, Z. Feng, D. Su, K. L. More, G. Wang, Z. Wang, G. Wu, *Nat. Catal.* **2018**, *1*, 935.
- [13] H. Fei, J. Dong, Y. Feng, C. S. Allen, C. Wan, B. Voloskiy, M. Li, Z. Zhao, Y. Wang, H. Sun, P. An, W. Chen, Z. Guo, C. Lee, D. Chen, I. Shakir, M. Liu, T. Hu, Y. Li, A. I. Kirkland, X. Duan, Y. Huang,

- Nat. Catal.* **2018**, *1*, 63.
- [14] M. Sun, J. Ji, M. Hu, M. Weng, Y. Zhang, H. Yu, J. Tang, J. Zheng, Z. Jiang, F. Pan, C. Liang, Z. Lin, *ACS Catal.* **2019**, *9*, 8213.
- [15] a) L. Yan, X. Zeng, S. Zhao, W. Jiang, Z. Li, X. Gao, T. Liu, Z. Ji, T. Ma, M. Ling, C. Liang, *ACS Appl. Mater. Inter.* **2021**, *13*, 8353-8360.; b) L. Yan, T. Liu, X. Zeng, L. Sun, X. Meng, M. Ling, M. Fan, T. Ma, *Carbon* **2022**, *187*, 145-152.
- [16] H. Zhang, S. Hwang, M. Wang, Z. Feng, S. Karakalos, L. Luo, Z. Qiao, X. Xie, C. Wang, D. Su, Y. Shao, G. Wu, *J. Am. Chem. Soc.* **2017**, *139*, 14143.
- [17] a) J. Ji, Z. Li, C. Hu, Y. Sha, S. Li, X. Gao, S. Zhou, T. Qiu, C. Liu, X. Su, Y. Hou, Z. Lin, S. Zhou, M. Ling, C. Liang, *ACS Appl. Mater. Inter.* **2020**, *12*, 40204.; b) Z. Li, Z. Wan, X. Zeng, S. Zhang, L. Yan, J. Ji, H. Wang, Q. Ma, T. Liu, Z. Lin, M. Ling, C. Liang, *Nano Energy* **2021**, *79*, 105430.; c) Z. Li, Z. Wan, G. Wu, Z. Wu, X. Zeng, L. Gan, J. Liu, S. Wu, Z. Lin, X. Gao, M. Ling, C. Liang, *Sustain. Mater. Techno.* **2021**, *30*, e333.
- [18] Y. Wang, H. Su, Y. He, L. Li, S. Zhu, H. Shen, P. Xie, X. Fu, G. Zhou, C. Feng, D. Zhao, F. Xiao, X. Zhu, Y. Zeng, M. Shao, S. Chen, G. Wu, J. Zeng, C. Wang, *Chem. Rev.* **2020**, *120*, 12217.
- [19] Z. Li, J. Ji, Q. Wu, D. Wei, S. Li, T. Liu, Y. He, Z. Lin, M. Ling, C. Liang, *Nano Energy* **2019**, 104234.
- [20] Y. Sha, J. Ji, S. Li, X. Gao, B. Zhang, M. Ling, C. Liang, Z. Lin, *Eur. J. Inorg. Chem.* **2019**, *13*, 287.
- [21] D. Liu, S. Ding, C. Wu, W. Gan, C. Wang, D. Cao, Z. U. Rehman, Y. Sang, S. Chen, X. Zheng, Y. Wang, B. Ge, L. Song, *J. Mater. Chem. A* **2018**, *6*, 6840.
- [22] Z. Zhu, H. Yin, Y. Wang, C. H. Chuang, L. Xing, M. Dong, Y. R. Lu, G. Casillas Garcia, Y. Zheng, S. Chen, Y. Dou, P. Liu, Q. Cheng, H. Zhao, *Adv. Mater.* **2020**, *32*, 2004670.
- [23] G. Chen, P. Liu, Z. Liao, F. Sun, Y. He, H. Zhong, T. Zhang, E. Zschech, M. Chen, G. Wu, J. Zhang, X. Feng, *Adv. Mater.* **2020**, *32*, 1907399.
- [24] J. Zhu, M. Xiao, G. Li, S. Li, J. Zhang, G. Liu, L. Ma, T. Wu, J. Lu, A. Yu, D. Su, H. Jin, S. Wang, Z. Chen, *Adv. Energy Mater.* **2019**, *10*, 1903003.
- [25] E. Hu, X. Yu, F. Chen, Y. Wu, Y. Hu, X. W. D. Lou, *Adv. Energy Mater.* **2018**, *8*, 1702476.
- [26] H. Fei, J. Dong, M. J. Arellano-Jiménez, G. Ye, N. Dong Kim, E. L. G. Samuel, Z. Peng, Z. Zhu, F. Qin, J. Bao, M. J. Yacaman, P. M. Ajayan, D. Chen, J. M. Tour, *Nat. Commun.* **2015**, *6*, 1.
- [27] a) B. Q. Li, C. X. Zhao, S. Chen, J. N. Liu, X. Chen, L. Song, Q. Zhang, *Adv. Mater.* **2019**, *31*, 1900592.; b) Y. Guo, P. Yuan, J. Zhang, Y. Hu, I. S. Amiinu, X. Wang, J. Zhou, H. Xia, Z. Song, Q. Xu, S. Mu, *ACS Nano* **2018**, *12*, 1894.; c) Y. Wang, B. Yu, K. Liu, X. Yang, M. Liu, T. Chan, X. Qiu, J. Li, W. Li, *J. Mater. Chem. A* **2020**, *8*, 2131.; d) L. Yang, L. Shi, D. Wang, Y. Lv, D. Cao, *Nano Energy* **2018**, *50*, 691.; e) X. Zhu, X. Tan, K. Wu, C. Chiang, Y. Lin, Y. Lin, D. Wang, S. Smith, X. Lu, R. Amal, *J. Mater. Chem. A* **2019**, *7*, 14732.; f) J. Han, X. Meng, L. Lu, J. Bian, Z. Li, C. Sun, *Adv. Funct. Mater.* **2019**, *29*, 1808872.; g) D. Ji, L. Fan, L. Li, S. Peng, D. Yu, J. Song, S. Ramakrishna, S. Guo, *Adv. Mater.* **2019**, *31*, 1808267.
- [28] a) M. Dong, X. Liu, L. Jiang, Z. Zhu, Y. Shu, S. Chen, Y. Dou, P. Liu, H. Yin, H. Zhao, *Green Energy Environ.* **2020**, *5*, 499-505.; b) K. Kordek, L. Jiang, K. Fan, Z. Zhu, L. Xu, M. Al Mamun, Y. Dou, S. Chen, P. Liu, H. Yin, P. Rutkowski, H. Zhao, *Adv. Energy Mater.* **2019**, *9*, 1802936.
- [29] V. Wang, N. Xu, J. Liu, G. Tang, W. Geng, *Comput. Phys. Commun.* **2021**, *267*, 108033.
- [30] B. Ravel, M. Newville, *J. Synchrotron Radiat.* **2005**, *12*, 537.
- [31] D. Chen, J. Ji, Z. Jiang, M. Ling, Z. Jiang, X. Peng, *J. Power Sources* **2020**, *450*, 227660.
- [32] G. Kresse, J. Furthmüller, *Comp. Mater. Sci.* **1996**, *6*, 15.
- [33] J. P. Perdew, K. Burke, M. Ernzerhof, *Phys. Rev. Lett.* **1996**, *77*, 3865.
- [34] P. E. Blochl, *Phys. Rev. B* **1994**, *50*, 17953.
- [35] a) S. Grimme, J. Antony, S. Ehrlich, H. Krieg, *J. Chem. Phys.* **2010**, *132*, 154104.; b) S. Grimme, S. Ehrlich, L. Goerigk, *J. Comput. Chem.* **2011**, *32*, 1456.
- [36] K. Momma, F. Izumi, *J. Appl. Crystallogr.* **2011**, *44*, 1272.

The introduction of Co, Rh or Ni atom leads to a more uniform distribution of Fe 3d orbital in dual-metal single-atom catalyst, weakening the binding energy of intermediates and reducing the energy barrier of the rate-limiting step in ORR/OER processes. Constructed catalyst enables outstanding electrocatalytic performances in bifunctional oxygen catalysis.

J. Ji, L. Wu, S. Zhou, T. Qiu, Z. Li, L. Wang,\* L. Zhang, L. Ma, M. Ling,\* S. Zhou,\* C. Liang

### Regulating electronic structure of single-atom catalysts towards efficient bifunctional oxygen electrocatalysis

